Geophysical Journal International

Geophys. J. Int. (2010) doi: 10.1111/j.1365-246X.2010.04805.x

Locating non-volcanic tremor along the San Andreas Fault using a multiple array source imaging technique

T. Ryberg,[1] Ch. Haberland,[1] G. S. Fuis,[2] W. L. Ellsworth[2] and D. R. Shelly[2]

[1] *Deutsches GeoForschungsZentrum Potsdam (GFZ), Telegrafenberg,* 14473 *Potsdam, Germany. E-mail: trond@gfz-potsdam.de*
[2] *U.S. Geological Survey,* 345 *Middlefield Road MS* 977, *Menlo Park,* CA 94025-3591, *USA*

Accepted 2010 September 7. Received 2010 August 31; in original form 2010 April 13

SUMMARY

Non-volcanic tremor (NVT) has been observed at several subduction zones and at the San Andreas Fault (SAF). Tremor locations are commonly derived by cross-correlating envelope-transformed seismic traces in combination with source-scanning techniques. Recently, they have also been located by using relative relocations with master events, that is low-frequency earthquakes that are part of the tremor; locations are derived by conventional traveltime-based methods. Here we present a method to locate the sources of NVT using an imaging approach for multiple array data. The performance of the method is checked with synthetic tests and the relocation of earthquakes. We also applied the method to tremor occurring near Cholame, California. A set of small-aperture arrays (i.e. an array consisting of arrays) installed around Cholame provided the data set for this study. We observed several tremor episodes and located tremor sources in the vicinity of SAF. During individual tremor episodes, we observed a systematic change of source location, indicating rapid migration of the tremor source along SAF.

Key words: Time series analysis; Body waves; Wave propagation; Continental tectonics: strike-slip and transform; Fractures and faults; North America.

1 INTRODUCTION

Strain release processes associated with the earthquake cycle find their expression in a diversity of different dynamic slip processes: 'conventional' earthquakes, slow earthquakes, continuous and episodic slip (silent earthquakes) and (non-volcanic) tremor episodes (e.g. Scholz 2002; Rubinstein *et al.* 2010). However, despite numerous observations, the physical mechanisms of non-volcanic tremor (NVT), which have been observed in subduction zones and strike slip environments since 2002, still remain unclear (e.g. Obara 2002; Rogers & Dragert 2003; Schwartz & Rokosky 2007; Rubinstein *et al.* 2008, 2010).

Tremor recordings are characterized by increased amplitude signals (with respect to seismic background noise) with durations of several minutes up to hours and with frequency content typically restricted to between 2 and 10 Hz. They do not show clear seismic body-wave arrivals, and it is, thus, difficult to locate tremor sources by conventional methods. However, knowledge of the location of the tremor sources (crust versus upper mantle, location relative to important interfaces and faults, etc.) and their evolution during a tremor episode remain as a key issue for understanding the physical mechanisms and the nature of NVT.

So far NVT has been localized using different approaches and different kinds of data sets (e.g. local or regional seismic networks). The first studies involved differential traveltimes of tremor recordings at network seismic stations using envelope-transformed and cross-correlated seismic traces. These traveltimes are further used in grid-search (or source-scanning) techniques to locate the source of the tremor (see e.g. Obara 2002; Nadeau & Dolenc 2005; Rubinstein *et al.* 2010). In contrast, Kao & Shan (2004) measured the 'brightness' of seismic traces projected onto candidate source locations together with a source scanning technique. Shelly *et al.* (2007a, 2006) showed that NVT in Japan contains low-frequency events (LFE) allowing to locate the tremor sources relatively by using a master event relocation technique thus yielding a high accuracy of the derived locations.

In addition to time reversal methods (Larmat *et al.* 2009), several attempts have been made to analyse tremor using seismic array techniques (e.g. La Rocca *et al.* 2005, 2008; Fletcher *et al.* 2008; La Rocca *et al.* 2010). In the following, the term 'array methods' is used for methods utilizing phase-consistent seismic signals observed by one or more cluster(s) (or arrays) of seismic stations (e.g. distributed at the Earth's surface; Fig. 1). The phase consistency of observations across several stations, which is usually not given in the case of coarse regional networks and high frequency signals, allows 'delay-and-sum' or stacking methods to be applied directly to the recorded seismograms and not to the envelopes, thus yielding potentially higher location precision.

Array methods have been widely used to study both (natural and artificial) seismic sources and Earth's structure. They were used to monitor nuclear explosions (e.g. Dahlman & Israelson 1977), to study the source processes of large earthquakes from teleseismic

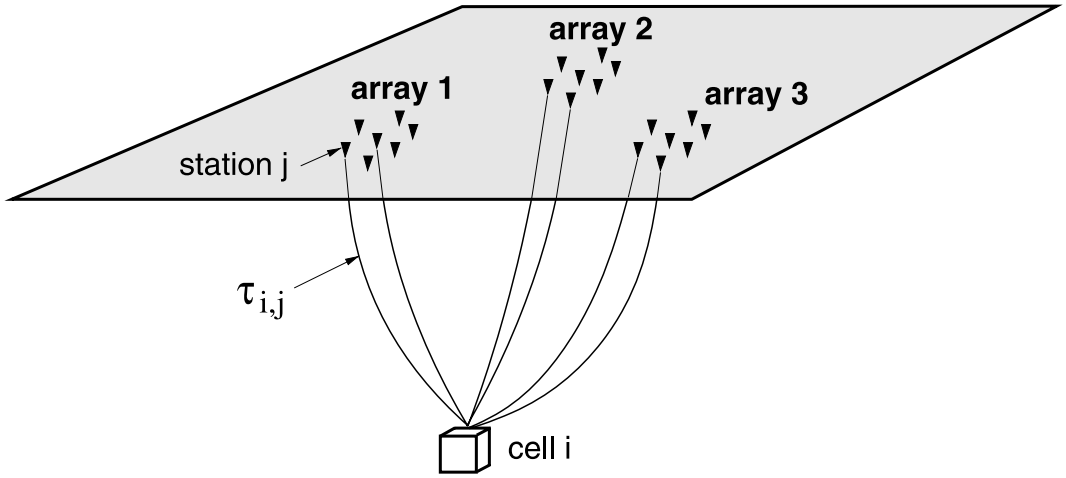

Figure 1. Sketch of the experimental layout showing a set of seismic arrays, a cell in the subsurface and rays with their associated traveltimes used to determine the tremor source locations.

distances (Krüger & Ohrnberger 2005a,b) and to locate the sources of volcanic tremor (Wassermann 1997; Almendros *et al.* 1999; Konstantinou & Schlindwein 2002; Chouet 2003). In addition, array studies proved to be successful to reveal subsurface structure at different scales, from the Earth's mantle and crust (Krüger *et al.* 1995, 1996, 2001; Weber & Wicks 1996; Scherbaum *et al.* 1997) to upper-crustal scatterers (Spudich & Bostwick 1987; Rietbrock & Scherbaum 1999; Vidale & Benz 1992) and shallow tectonic faults (Maercklin *et al.* 2004). Depending on acquisition geometry and source–receiver distances, plane or curved wave front approaches are used in the analysis.

For NVT analysis, plane waves are used to measure the slowness vector or azimuth and slowness (e.g. La Rocca *et al.* 2005; Fletcher *et al.* 2008). Array techniques in combination with determined *P*- minus *S*-wave traveltimes of tremor events have been used to locate tremor sources in Cascadia (La Rocca *et al.* 2009; Ghosh *et al.* 2009). La Rocca *et al.* (2008, 2010) used the measured slowness vectors to further estimate the tremor source position in a probabilistic source location approach.

To study the NVT at the San Andreas Fault (SAF), we conducted a seismic experiment in the Cholame, California region. During Fall 2007, we deployed four small-aperture seismic arrays near the SAF for a time period of 6 weeks (Fig. 2). In this time, 70 episodes of tremor activity occurred in the region. Using this array data set and the recordings at regional seismic stations, Shelly *et al.* (2009) and Shelly (2009) were able to identify an LFE within the tremor wavetrain. The LFE hypocentre was calculated from *S*- and *P*-arrival times. Other portions of the tremor resembling the waveform of the LFE were then located relative to the LFE. All tremor sources were found to be located beneath the SAF and near the Moho at a depth of ∼26 km.

Plane-wave array analysis of single arrays yielded very stable backazimuth and slowness values which motivated us to combine the NVT observations at several arrays to locate the tremor sources and track movement of the sources within a single tremor episode.

In this paper, we describe a multiple array imaging approach that is similar to Kirchhoff migration (imaging) known from reflection seismic exploration and which directly combines specific aspects of methods mentioned earlier (e.g. source scanning, analysis of phase consistent signals). The validity and potential of the proposed array method is shown with synthetic data sets. Limitations and possible problems of the technique will be evaluated and discussed when applied to SAF data.

2 EXPERIMENT

Each of the four small-aperture seismic arrays deployed in 2007 near the SAF consists of 10 seismic stations located within an area of roughly 1 km diameter (Fig. 2). Distances between the arrays vary between 15 and 50 km. Although two of the arrays (A2, A3) are designed for optimal performance following Haubrich (1968), one array (A1) consists of irregularly positioned stations and the L-shaped fourth array (A4) was constrained by site access considerations. All seismic stations of arrays A1–A3 were equipped with a short period (4.5 Hz) three-component seismic sensors and a GPS-synchronized data loggers, recording continuously at a sample rate of 200 sps. Array A4 was equipped with 2 Hz sensors and recorded at 250 sps. A complete list of all station coordinates is found in Appendix B. During the 6-week experiment, several episodes of tremor activity occurred in the region. Fig. 3 shows a typical record of the vertical component recording of a tremor at all arrays.

The directional sensitivity and resolution power of an individual array is described by the array transfer function (ATF, Harjes & Henger 1973). Fig. 4 shows the array design and the corresponding ATFs. Due to the optimal setup, the ATFs of arrays A2 and A3 are characterized by a sharp main lobe and insignificant side lobes indicating an excellent directional selectivity. Array A1 shows a generally sharper main lobe due to the larger aperture ($>$1000 m) and a series of small amplitude side lobes which appear not to affect the imaging results (see synthetic tests later). Array A4 shows an elongated main lobe due to its L-shaped set-up.

3 PLANE-WAVE ARRAY ANALYSIS

To detect tremor, we used a plane-wave beam forming approach similar to Ghosh *et al.* (2009) to measure the azimuth and apparent velocity of the most coherent signals arriving at an array (Appendix A). Directional information for each individual array was sequentially measured in moving time windows of 8 s for the band-passed vertical component recordings (4–16 Hz, where most of the tremor energy was observed). Our criteria for tremor detection is that at

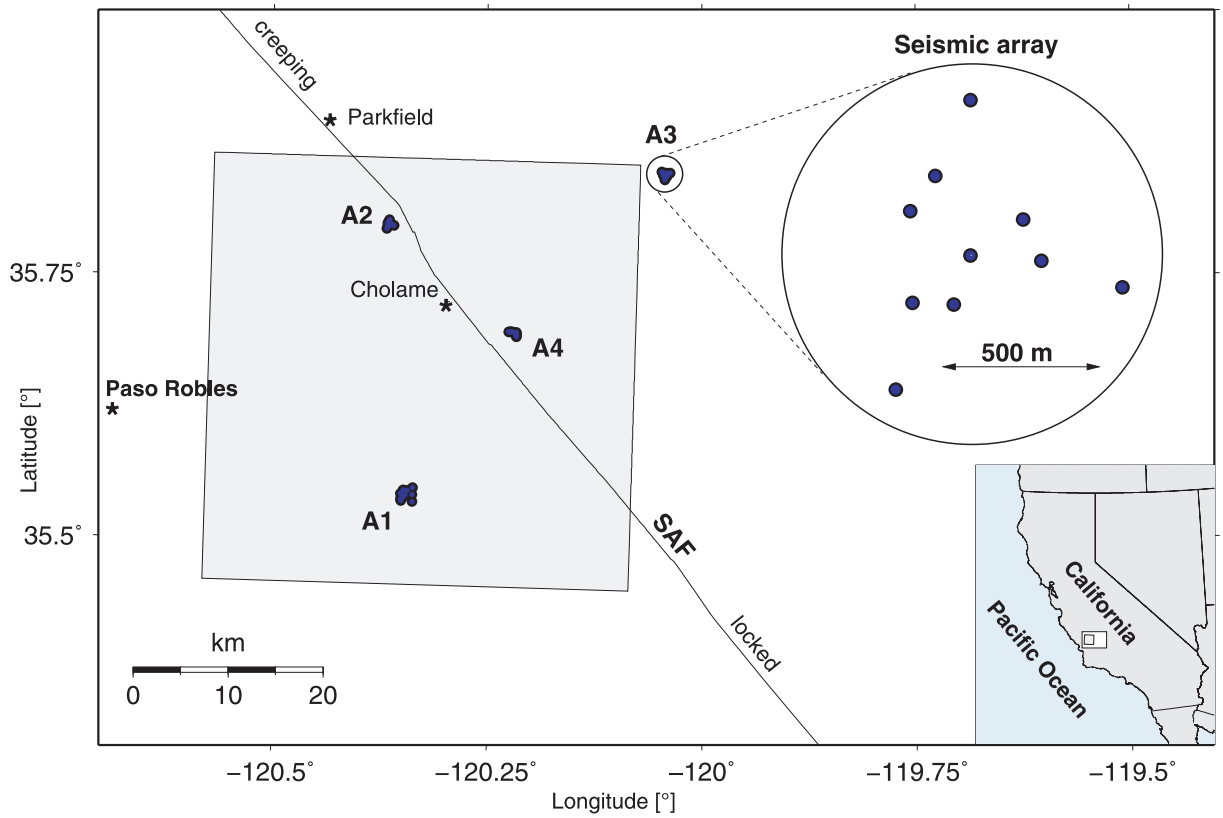

Figure 2. Map of the study area along the San Andreas fault (SAF) near Cholame, CA (USA). A1, A2, A3 and A4 indicate the location of the small-aperture arrays, the inset shows the individual array design (A3). The box is the search box for the tremor sources. See Appendix B for coordinates.

least one of the arrays shows (1) sufficiently small slownesses (energy coming from below), (2) energy arriving from approximately the expected azimuths and (3) at least some elevated semblance values. In the case of tremor, the directional information should be stable for several consecutive time windows. During 6 weeks of continuous recording, we identified more than 70 tremor episodes of different strength with this method. Fig. 5 shows an example of a tremor record and the derived changes in slowness, azimuth and semblance associated with it.

As shown in Fig. 5, immediately before and after the event these derived quantities are random, and likely reflect the properties of seismic noise (mainly scattered surface waves). With the onset of tremor energy, the calculated azimuth stabilizes, the slowness reaches values characteristic for a deeper source and the semblance values indicate detection of coherent energy within the array. One interesting observation is that the azimuth of the tremor changes slowly during its occurrence, indicative of a moving source. The tremor has a rather high-frequency content between 4 and 20 Hz, however, the lower bound might reflect recording limitations of the deployed seismic sensors. It is interesting to note that the actual amplitude of the events does not directly correlate with the tremor detections, that is those tremor events with the strongest amplitude do not necessarily show the most stable directional and coherency information. This suggests that multiple source locations are radiating at the same time during high-amplitude tremor episodes. Somewhat surprisingly, semblance values do not reach high values, but are rather small (<0.2). This might be explained by small time delays caused for instance by small variations of shallow subsurface velocities, in combination with the high frequencies analysed for tremor resulting in out-of-phase tremor signals. At the same time, microseismic signals at 5 s period and originating in the Pacific, which were also analysed for test purposes, reach semblance values >0.8 and directions pointing toward the ocean, thus supporting the performance of the array processing technique. We found that neither the choice of the seismic component, the frequency band analysed, or the length of the time window had a significant influence on the array analysis results.

4 MULTIPLE ARRAY SOURCE IMAGING TECHNIQUE (MASI)

Assuming a set of seismic arrays (Fig. 1), we present a Kirchhoff-style imaging technique to determine source locations of NVT. For all times T (which are possible tremor origin times), we scan the gridded subsurface, calculate the traveltimes $\tau_{i,j}$ from each cell i to the stations j (N is number of stations for a given array) assuming a known velocity model (a model similar to Nadeau & Dolenc (2005), see Appendix D), shift the traces (horizontal or vertical component) according to the calculated traveltimes and estimate the coherency or similarity of the observed waveforms x_j within a corresponding (small) time window Δ across the array stations. This is separately performed for each array k (M is number of arrays) and for all subsequent time windows. We invoke the semblance function as a measure of signal similarity or coherency (Taner & Koehler 1969; Neidell & Taner 1971) as similarly applied in previous array studies (e.g. Lay 1987; Rietbrock & Scherbaum 1999; Maercklin *et al.* 2004). The semblance can be interpreted as the beam power,

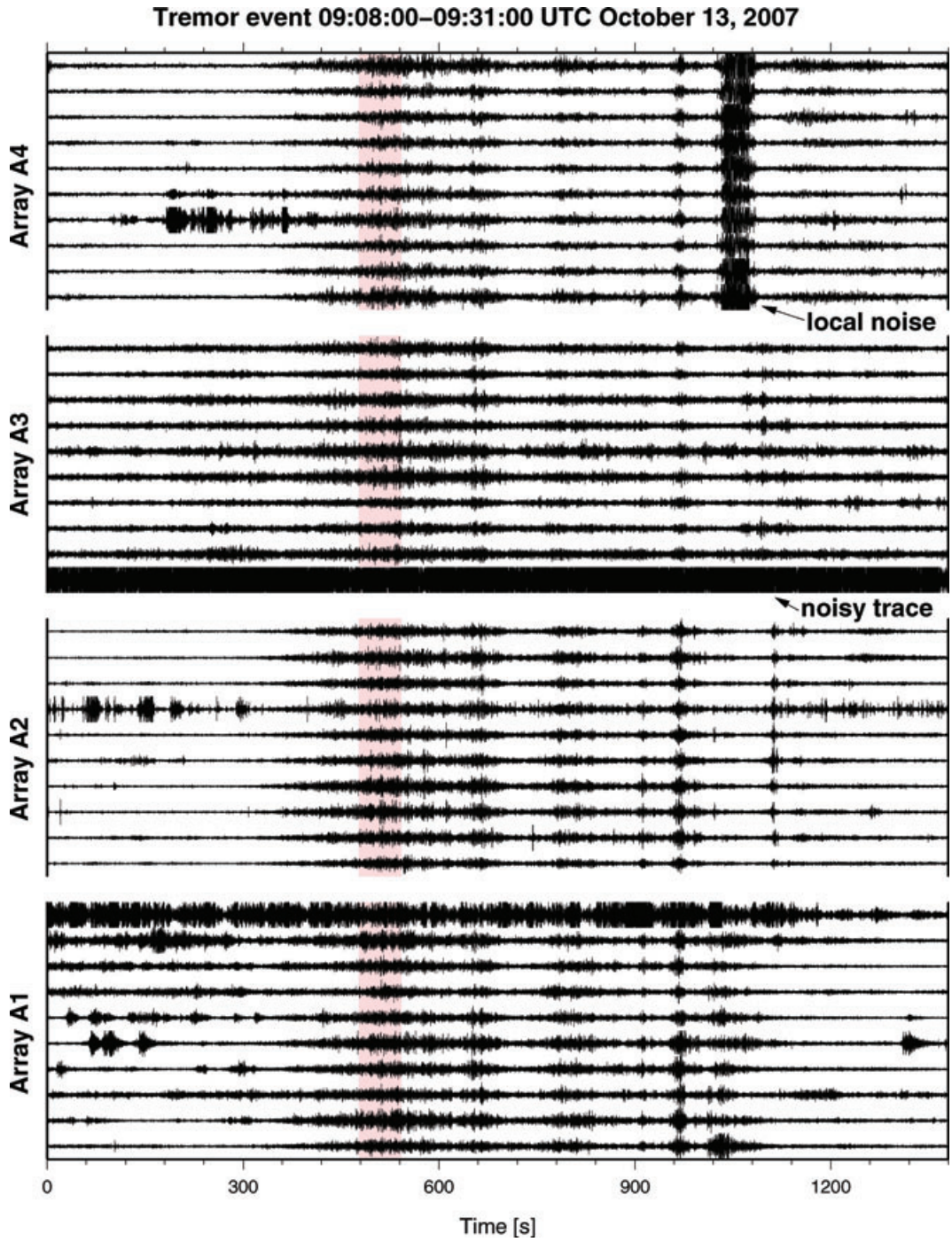

Figure 3. Complete example of a tremor event from 2007 October 13, 09:08 UTC, recorded at all four arrays (vertical component, band-passed seismograms). The light-pink zone is further analysed in Fig. 9. Although some of the traces are noisy, the tremor event is clearly seen on all arrays.

normalized to the power of the individual traces. If data of all stations are perfectly coherent, the semblance has a value of 1:

$$S_{i,k}(T) = \frac{\sum_{t=T-\Delta/2}^{T+\Delta/2} \left(\sum_{j=1}^{N} x_{k,j}(t+\tau_{i,j}) \right)^2}{N \sum_{t=T-\Delta/2}^{T+\Delta/2} \sum_{j=1}^{N} x_{k,j}^2(t+\tau_{i,j})}. \quad (1)$$

In a second step, the resulting spatial semblance distributions $S_{i,k}$ for each array and each time step are combined (combined semblance, $CS_i(T)$) in a multiplicative way (geometric mean):

$$CS_i(T) = \sqrt[M]{\prod_{k=1}^{M} S_{i,k}}, \quad (2)$$

where M is the number of arrays. Other combinations of the individual semblances S are possible, that is arithmetic averages, median, etc. Arithmetical means were tested and resulted in very similar tremor locations. The cell with the highest combined semblance CS is then interpreted as to reflect the most likely location of the source. Choosing the cell with the highest semblance value (CS) is based on

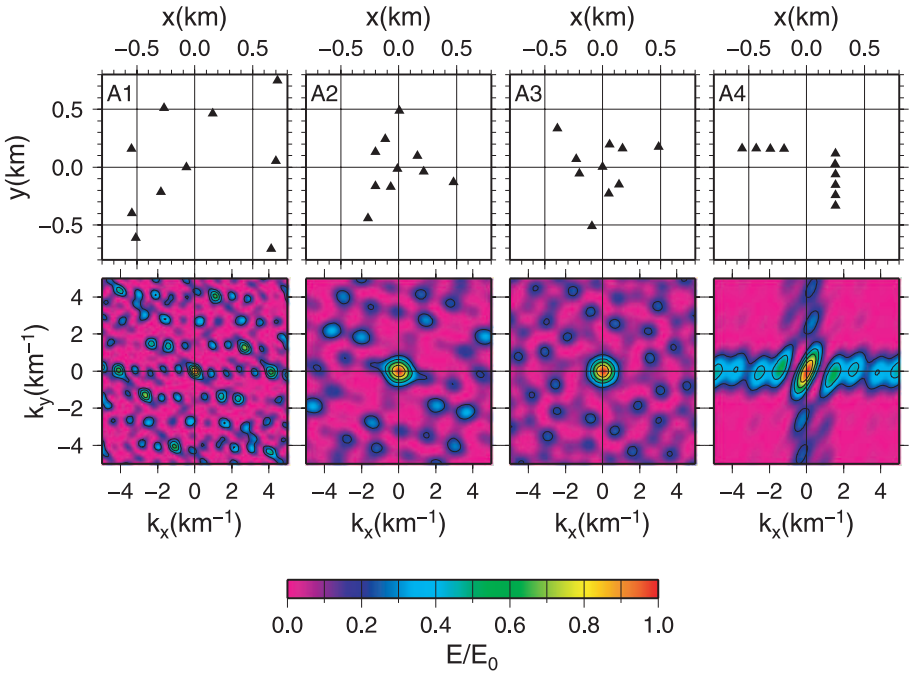

Figure 4. (Top panel) Geometries of the small-aperture arrays A1—A4 (left to right). Arrays A2 and A3 (aperture 1000 m) resemble an almost optimal set-up following Haubrich (1968). Because of logistical reasons, array A1 exhibits an irregular geometry (aperture ∼1400 m) and array A4 (aperture ∼1000 m) is L-shaped. Absolute locations are shown in Fig. 2; see also Appendix B. (Bottom panel) Array transfer functions (ATF) for all arrays (at 1 Hz). Beam energy as a function of wavenumber k is colour coded. See text for details.

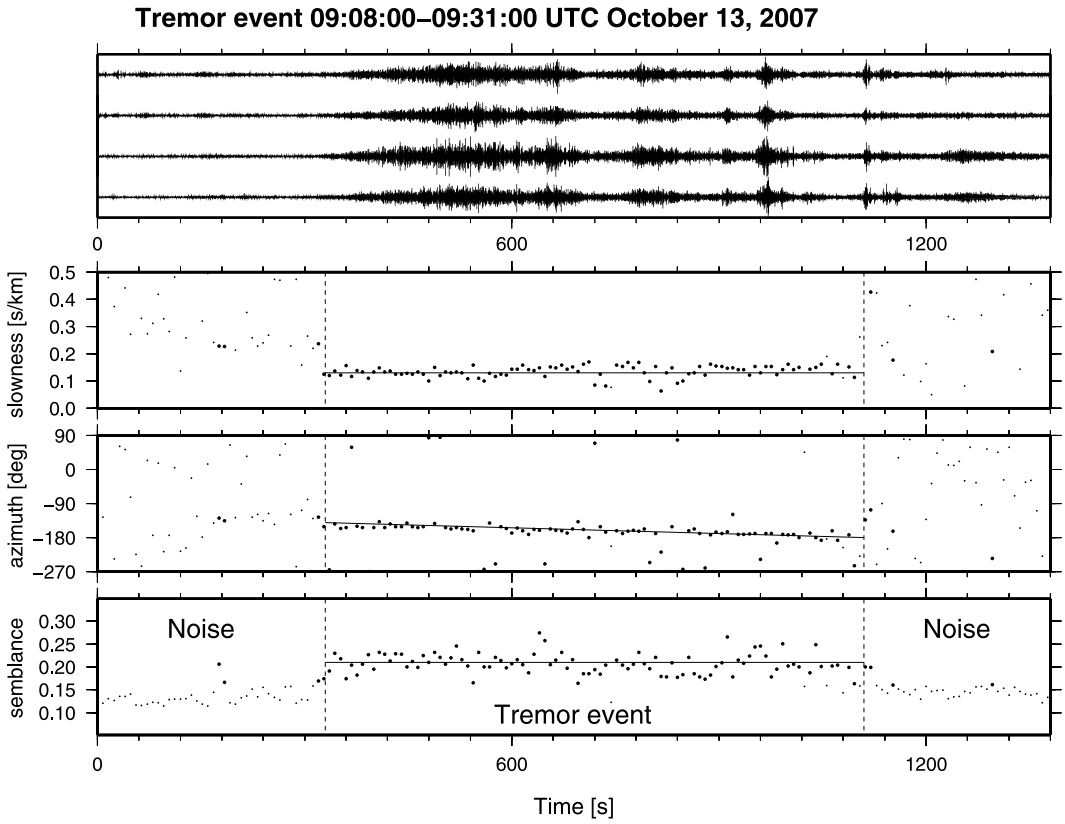

Figure 5. (Top panel) Example seismograms for typical tremor episode (vertical component, band-passed seismograms for stations at array A2). (Bottom panel) Results of the directional analysis (in moving time windows of 8 s), for slowness, azimuth and the signal semblance. The first 5 and last 4 min are characterized by random azimuths, high slowness and low semblance values, indicative of seismic background noise. During the tremor event, the semblance increases (emphasized black circles with semblance >0.16), the slowness decreases and azimuths show energy arriving at the array from below at a specific azimuth. Note the progressive change of azimuth during the tremor episode indicating a moving tremor source.

the underlying assumption of one point source emanating seismic energy at one time. If one expects spatially distributed sources or more sources acting simultaneously, other techniques than selecting the cell with the maximum semblance have to be applied (i.e. the whole semblance distributions have to be considered). The traveltime $\tau_{i,j}$ was calculated by an eikonal solver through an appropriate velocity model (Vidale 1988, 1990).

The underlying concept of this imaging technique is very similar to pre-stack Kirchhoff-style imaging well known from controlled source reflection seismics (see, e.g. Schneider 1976; Buske 1999) or to beam-forming (e.g. Spudich & Bostwick 1987; Krüger *et al.* 1993; Scherbaum *et al.* 1997; Rietbrock & Scherbaum 1999; Maercklin *et al.* 2004) with the difference that the location of the sources themselves are imaged, instead of scatterers or reflective elements (see, e.g. also Rentsch *et al.* 2007).

The presented method requires a set of arrays forming a multi-scale array. The individual small-aperture arrays provide observations of coherent signals necessary for stacking techniques ('small' compared to the predominant wave-length). The large spacing between individual arrays (a set of individual small-aperture arrays) is important for the determination of the epicentre and the source depth. Ideally, the array aperture should be at least in the range of the depth of the sources.

5 SYNTHETIC EXAMPLE AND EARTHQUAKE RELOCATION

5.1 Synthetic example

To demonstrate the performance of our technique, we calculate synthetic traces for the given source and receiver distribution and apply the imaging method outlined earlier. The hypothetical receiver distribution in the example mimics the true distribution of receivers of an experiment at the SAF near Cholame, the hypothetical source position is arbitrarily chosen within the region of the array. The synthetic signal of each trace used is a sinusoidal wave train (10 Hz, length 20 s), which is shifted according to the traveltimes from the given source position to the receiver thus resulting in a set of synthetic traces. Any other source time function, as long as it is coherent across an array would give similar results with MASI, because the array technique relies exclusively on the coherency of the signal instead of the specific waveform. Ray tracing is done in an assumed 1-D velocity model by finite difference traveltime calculation following Podvin & Lecomte (1991) and Schneider *et al.* (1992). In this application of the MASI technique, we used a scanning volume (45 × 45 × 45 km) and subdivided the subsurface into cells of 0.5 km horizontal and 1 km vertical size.

Fig. 6 shows the slices of the individual and combined semblance volumes (*S* and *CS*, respectively) at the position of the source locations. The distribution of the individual array-semblances *S* show a distinct peak indicating the tremor source position (crosses in Fig. 6A). Differences in broadness and shape of the semblance distributions for the four arrays *S* reflect different source–receiver distances, slightly different aperture of the arrays and different array transfer functions due to different receiver array geometry. This is particularly obvious for array 4 featuring an elongated main lobe due to its asymmetric L-shaped set-up which corresponds to the elongated (SW–NE trending) peak of the semblance distribution *S* (Fig. 6A). The elongation of the main lobe of the semblance distributions for array A3 is mainly caused by the larger distance to the source.

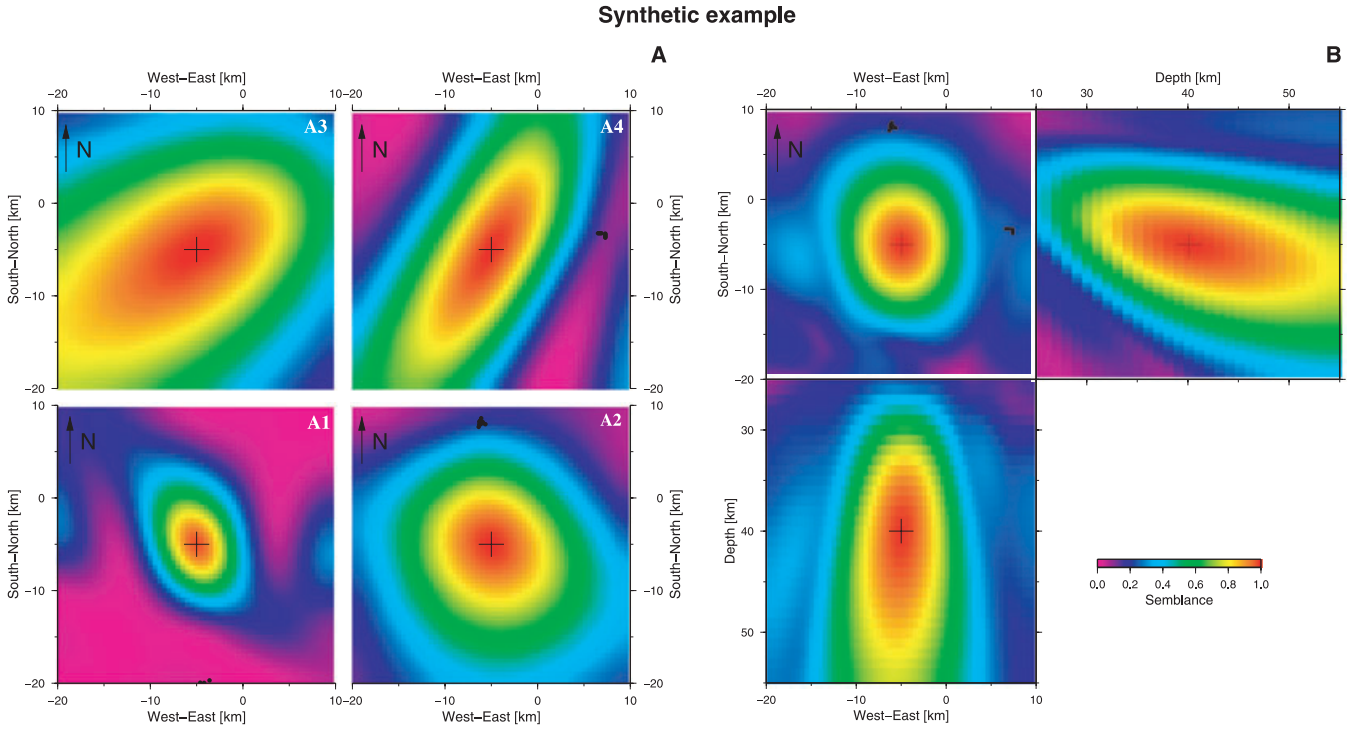

Figure 6. (A) Horizontal slices through the semblance volumes *S* of arrays A1–A4, for a noise free synthetic event. Note that all arrays have their maxima consistently at the source location indicated by crosses. (B) Slice through the combined semblance volume *CS* of all arrays. The 3-D semblance volume is sliced at the position of the maximum, indicated by crosses which coincides with the recovered source location. The shape of elevated semblance values shows a well-developed peak in map view, equivalent to high-potential horizontal resolution. The elongated shape in depth is indicative for lower accuracy of depth determination.

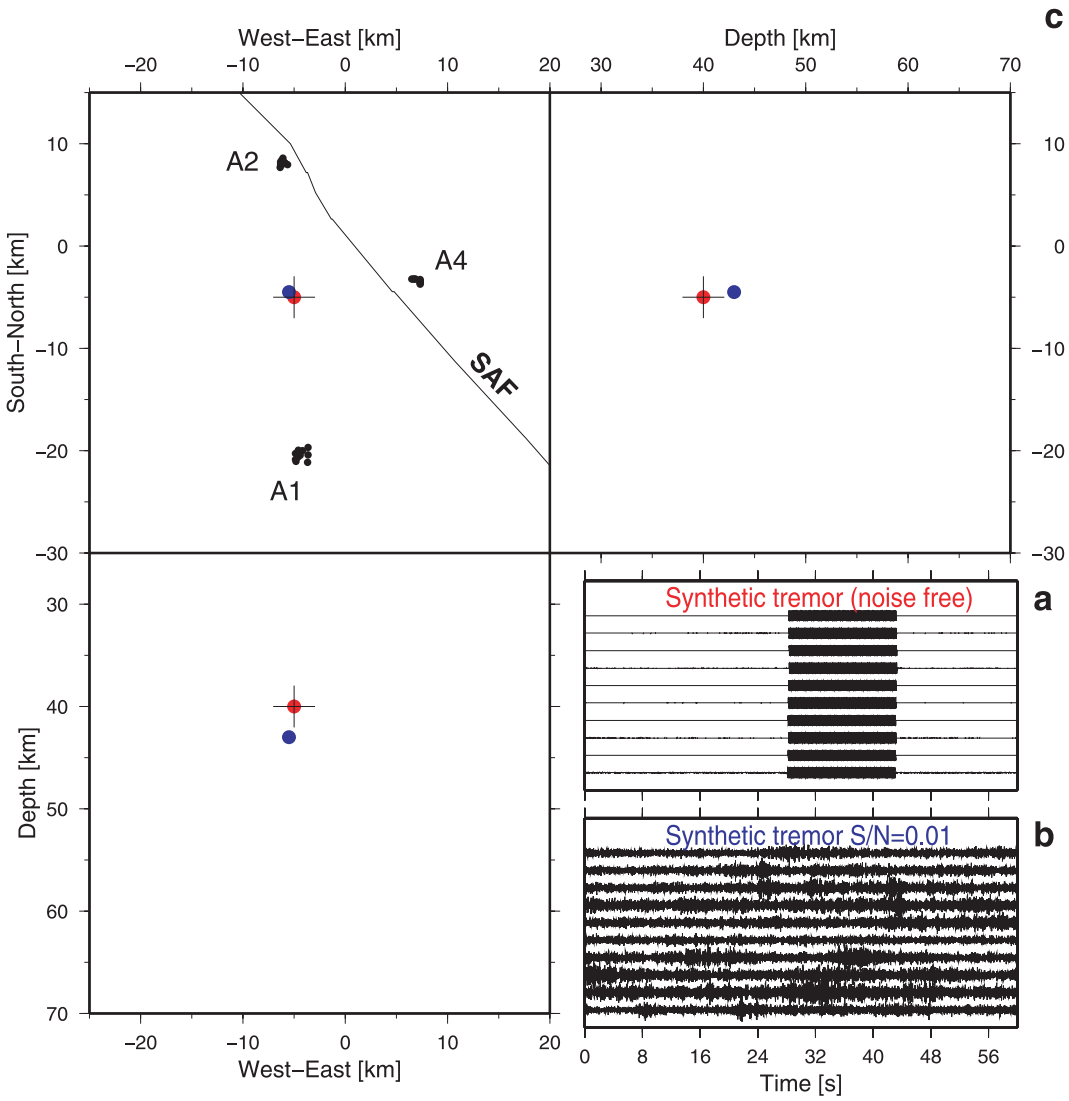

Figure 7. Two examples of tremor localization for synthetic data examples. The lower right panels (A and B) show the synthetic waveform data (top, noise free; bottom, with S/N-ratio of 0.01) for array A1. (C) Shows the result of the search for tremor location (projections), crosses indicate the original position, coloured dots show the locations of the noise free (red) and noisy data set (blue). Note that while the horizontal positions for both data sets could be recovered with high resolution, the depth of the hypocenter for the noisy data set is offset by 4 km. This is consistent with the high horizontal and lower vertical resolution of our method.

In the combined semblance *CS*, the peak is focused in the map view; in the depth section, the peak is slightly vertically elongated, indicating a reduced resolution of the derived source depths (Fig. 6B). However, through application of the MASI technique (using the same velocity model as used in the calculation of the synthetics) the source location could be perfectly recovered (Figs 7A and C, red dots), that is for more realistic conditions, we added noise to the synthetic traces, assuming a *S*-wave source and velocity model. We used the recordings of a tremor-free period as a realistic source of seismic noise. The individual noise traces had been added to the scaled synthetics, resulting in a very low signal-to-noise ratio (S/N) of 1:100 (Fig. 7B). Even for this very poor S/N-ratio, the MASI method resulted in surprisingly good source location recovery, particularly of the epicentre (Fig. 7C, blue dots). We are aware of the fact that the relatively short and monochromatic signal of a non-moving source, in contrast to our observations, might limit the evaluation of this synthetic test.

5.2 Earthquake relocation

To assess the location accuracy of MASI, we used the same method to locate local earthquakes and compare the derived hypocentre parameters to those reported by the California Integrated Seismic Network (http://www.cisn.org). During our observational phase, several small earthquakes were recorded within and outside, but near, our four arrays. To locate them, we used an adjusted scanning volume. Fig. 8 shows the result of our earthquake location using MASI, compared to the catalogue location. For the event within the arrays (near Cholame), we could recover the epicentre, although the off-array event seems to be offset by a few kilometres with respect to the catalogue location (Fig. 8).

As discussed earlier, the depth is less well resolved. Keeping in mind that the MASI described here only uses *S*-wave information, compared to *P*-wave (and *S*-wave) traveltimes used to derive catalogue locations, MASI performs surprisingly well. However, the

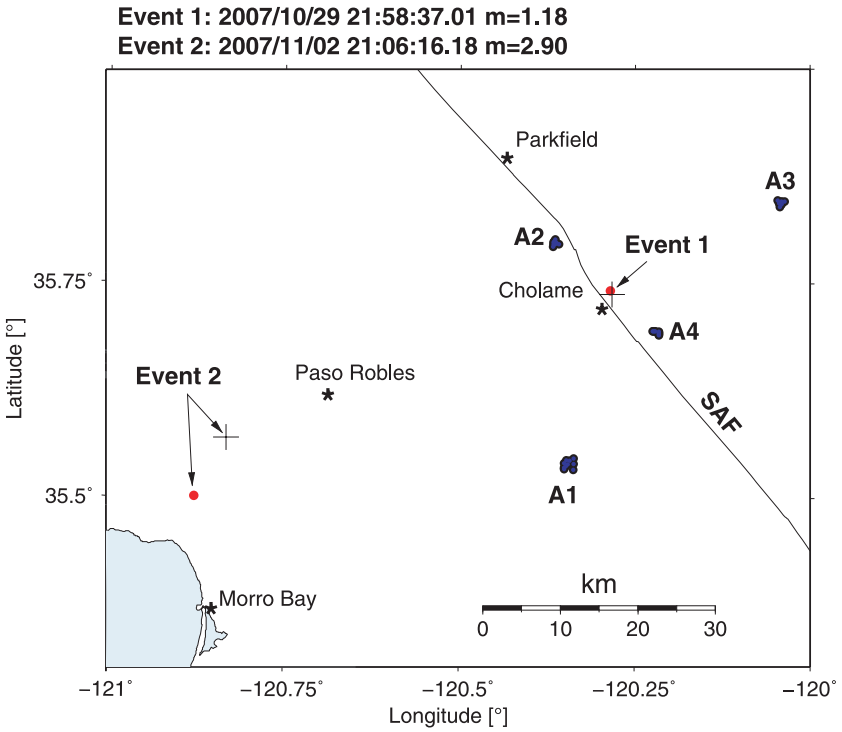

Figure 8. Crosses indicate the location of the two small earthquakes (California Integrated Seismic Network (http://www.cisn.org)). Red circles show the epicentres determined by our array method. The location of event 1 could be recovered with high accuracy, because it is inside of the cluster of our arrays. Event 2 is located far outside of the array cluster, but still could be located with an accuracy of <10 km. Note that for the MASI location of the earthquakes no traveltime but only directional and slowness.

frequency content, event duration and, importantly, focal depth of the local earthquakes used in this test differ from those of the tremor events. Therefore, the matching of the earthquake hypocentres by MASI does not necessarily mean that the NVT can be located with the same precision.

6 MASI APPLICATION TO SAF DATA

To determine the location of the sources of the detected tremor at the SAF at Cholame, we applied the MASI technique outlined in Section 4 to 70 tremor episodes. As in the synthetic example, we chose a scanning volume of 45 × 45 × 45 km and subdivided the subsurface into cells of 0.5 km horizontal and 1 km vertical size. Because the 3-D velocity model of Thurber *et al.* (2006) is poorly resolved in the tremor region around Cholame, we used the 1-D *P*-wave velocity model of Poley & Eaton (ftp://ehzftp.wr.usgs.gov/klein/crustmodels) as it is very similar to the average 1-D model of Thurber *et al.* (2006). From this model, we derived the *S*-wave model by scaling the *P*-wave model by 1.73, because the tremor energy is often assumed to consist mainly of *S* waves (Kao & Shan 2004; Kao *et al.* 2005; Nadeau & Dolenc 2005). The latter assumption is supported by the observation of Shelly *et al.* (2009), who has shown a data example of a LFE event (part of tremor) where *S* phases have the largest amplitudes even on the vertical component recordings. For further discussion of the issue of *P*- or *S*-wave velocity model, see Section 7.2. Simple elevation statics we used as a first approximation to site corrections (Appendix C; for detailed discussion see Section 7.1). The technique is then applied to subsequent time windows of 60 s length which are shifted by 60 s; no window overlap is considered.

Fig. 9 shows the slices of the individual and combined semblance volumes (*S* and *CS*, respectively) for the tremor event shown in Fig. 5 (time window indicated in Fig. 3). As in the synthetic example, the semblance distributions *S* for the individual arrays show distinct peaks (indicated by red colours in Fig. 9), however, the peaks have different shapes for different arrays. Array A3 is associated with a rather broad maximum possibly related to the relatively large epicentral distance. The peak in the array A1 distribution is strongly focussed. Similarly to the synthetic example, array A4 shows an elongated peak (in WSW–ENE direction) which is most likely directly related to its L-shaped station distribution. Array A2 shows a prominent secondary peak possibly indicating multipathing or reflections, however, this issue is not fully understood.

Again, we assume that the maximum of combined semblances *CS* indicate the most likely location of the tremor source. The distribution of *CS* shows a focussed peak in map view; vertically the maximum is smeared out, which again indicates a limited depth resolution. The results of the localization of all detected and located tremor are summarized in Fig. 10. The locations of the maxima of the combined semblances *CS* in each time window are indicated by circles. We found that almost all tremor occur in a narrow zone, no more than a few km wide, striking subparallel with the SAF and centred about ∼14 km southwest of the surface trace of the SAF. The tremor depths are typically 40 km, which is in the depth range of 20–40 km given by Nadeau & Dolenc (2005). Our tremor locations form a spatial cluster similar to that derived by Shelly *et al.* (2009), but the latter locations are about 1 km northeast of the surface trace of the SAF and at ∼26 km depth.

In addition to the analysis of the vertical seismic component data, we also looked at the horizontal component data recordings

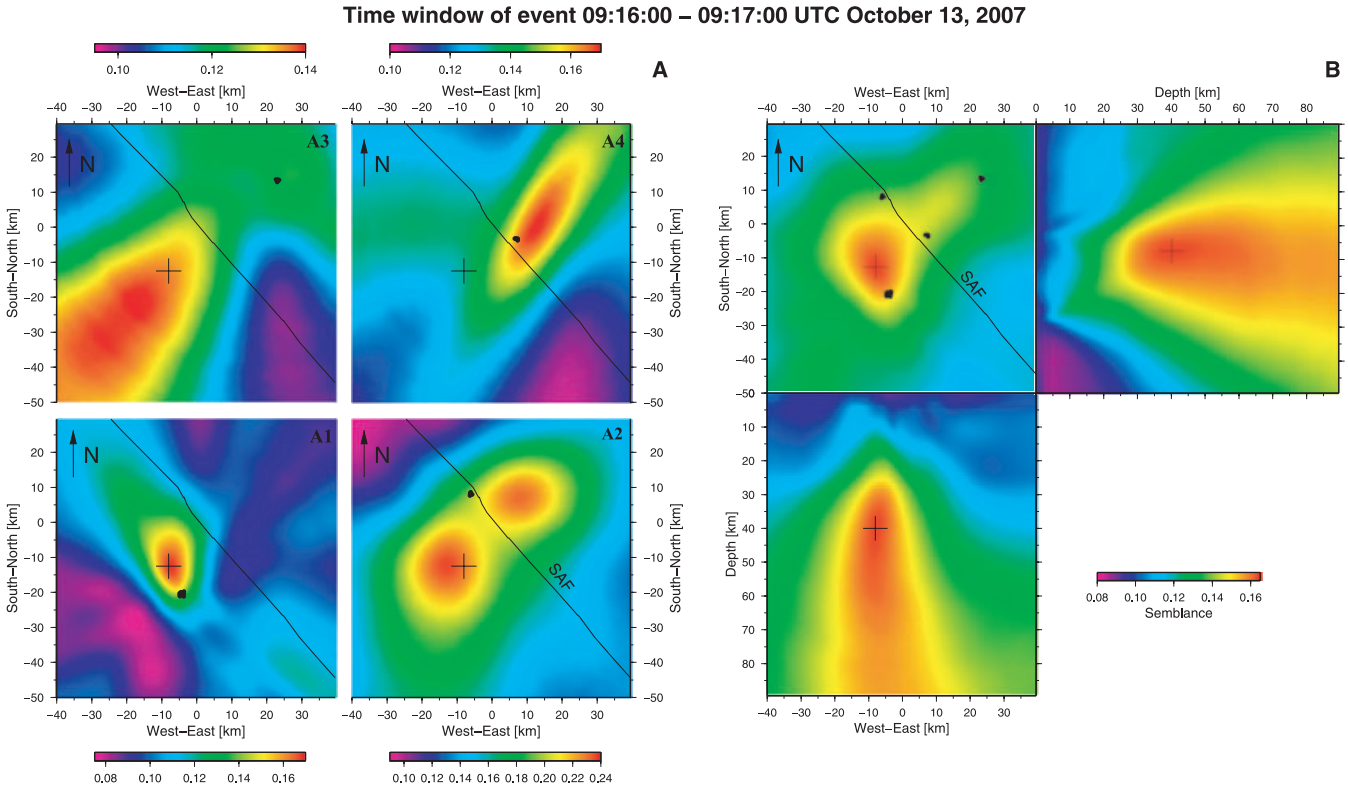

Figure 9. (A) Horizontal slices through the semblance volumes *S* of arrays A1–A4, for event 2007 October 13, 09:08 UTC, time window 09:16–09:17 (pink region in Fig. 3) at the depth of 40 km, centred at 120°17.81′W and 35°43.42′N. Every diagram has its individual colour scale. Note that arrays A1, A2 and A3 point consistently to the potential source location SW of SAF. Array A2 indicates that a second source region northeast of SAF is active simultaneously (or multipathing/reflection occurs), and A4 points to a source northeast of SAF. (B) Slice through the combined semblance volume *CS* of all arrays. The 3-D semblance volume is sliced at the position of the maximum, indicated by crosses. The search space is much larger than actually used for the analysis of the complete tremor data set. It shows that outside the search volume no semblance extrema exist, especially at depth <30 km. The shape of elevated semblance values shows a well-developed peak in map view, equivalent to high-potential horizontal resolution. The elongated shape in depth is indicative of weaker control on tremor depth.

and performed a source localization. Surprisingly, the coherence of tremor signals appear to be slightly larger on the vertical than on the horizontal components, which might reflect higher noise levels at the horizontal components. However, the corresponding tremor source locations coincide with those derived from the vertical component, although, their spatial scatter is slightly larger.

7 POSSIBLE INFLUENCING FACTORS

The location of tremor sources made with elevation statics lie approximately ∼14 km southwest of and parallel to the SAF, and obviously contrasts with the locations of Shelly *et al.* (2009) and Shelly (2009). Nadeau & Dolenc (2005) found locations with ∼7 km offset from SAF, which splits the difference between our and the locations of Shelly *et al.* (2009). In the following, we explore some possible resolutions. Finally, we present a calibration procedure based on the NVT locations by Shelly *et al.* (2009).

Waveform distortions due to a complex subsurface structure could yield local ray bending effects or multipathing (or multiple simultaneous sources) resulting in differential time delays at the array stations, which affect the derived azimuths and slownesses and could finally result in shifted locations of the seismic sources. These effects are observed from regional broadband arrays (e.g. Krüger & Weber 1992; Weber 1994) and from small-aperture arrays (e.g. Schweitzer 2001).

Complex structures at the SAF are well known at Parkfield (Ben-Zion & Malin 1991; Thurber *et al.* 2006). Further evidence for a complex structure in the Parkfield region comes from reflection and refraction seismic imaging showing strong lateral velocity contrast across the SAF system (e.g. Thurber *et al.* 2003, 2006; Hole *et al.* 2006). Unfortunately, the velocity model of the SAF region around Cholame of Thurber *et al.* (2006) is poorly resolved in the tremor region. In addition, the very shallow site structure can produce significant time delays (not accounted for in the elevation statics) that could also contribute to systematic mislocations.

7.1 Elevation and residual statics

To take into account different receiver elevations of individual stations within one array elevation static corrections have to be applied. To quantify the elevation static corrections based on a simple homogeneous velocity model, we searched for an array specific optimal correction velocity. We systematically varied the elevation static correction velocity for a selected tremor event and looked for the average semblance. We found values of 650 m s^{-1} (array A2) and 1000 m s^{-1} (arrays A1, A3, A4) optimal, thus maximizing the averaged semblance values for a tremor event. Appendix C shows a table of the individual elevation static corrections. Elevation static correction velocities other than the optimal values resulted in slightly shifted tremor sources locations (a few km horizontally). Generally,

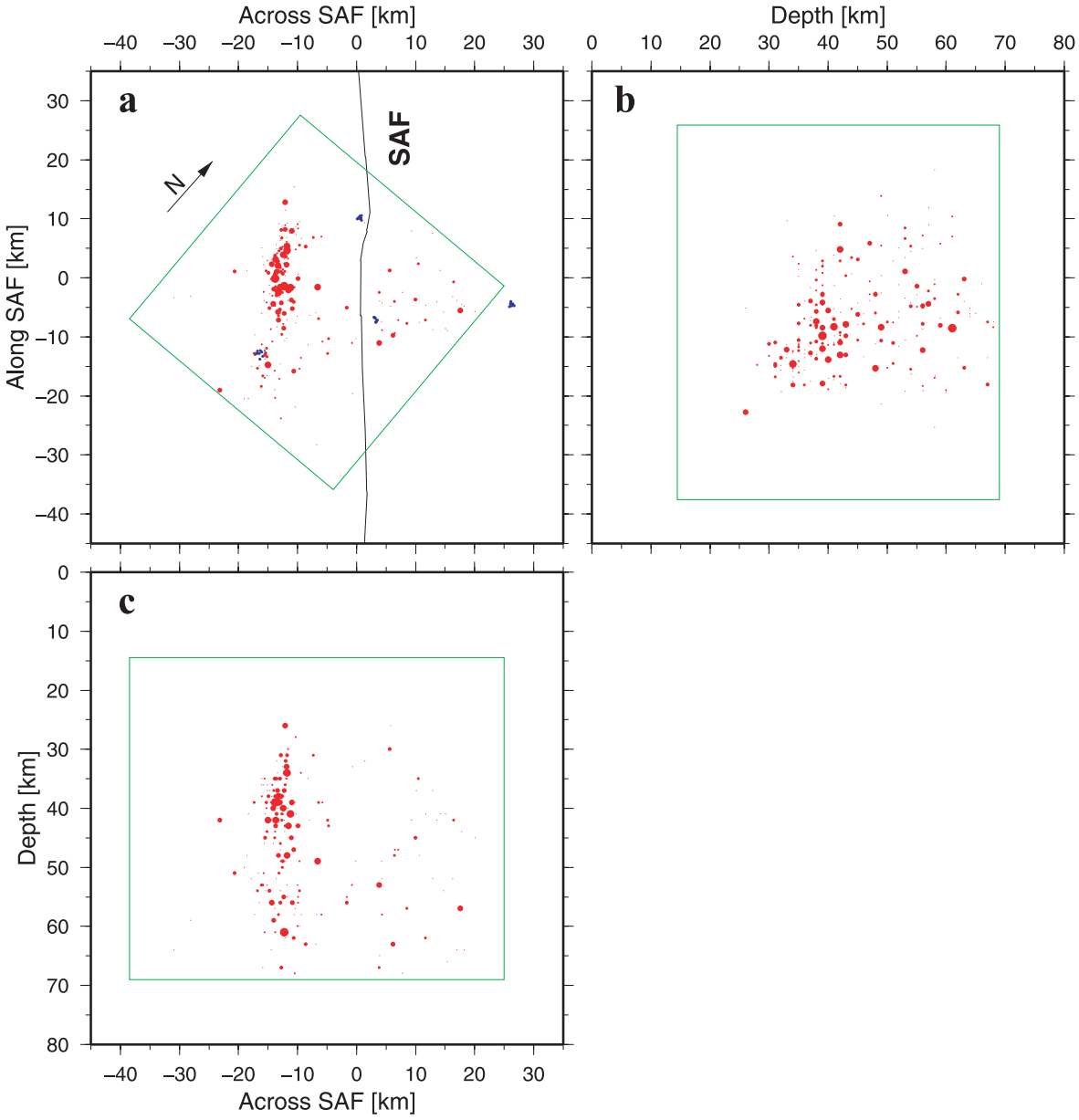

Figure 10. Rotated projection (map view centred at 120°17.81′W and 35°43.42′N and two side views) of tremor locations made with elevation statics for all events. Note that the majority of the tremor sources are concentrated in a segment of ∼20 km length and are aligned with the surface trace of the SAF at an offset of ∼14 km. The depth of the tremor sources lies between 30 and 60 km in the upper mantle of the Earth and is curtain-shaped. Depth determination is of lower precision than the epicentral position.

the application of the elevation static corrections resulted in slightly different tremor source locations with less spatial scatter. A similar search for any remaining residual static correction was carried out and resulted in very small values (typically less than one, not exceeding two samples or 0.01 s) and thus had been neglected during further data processing.

7.2 Velocity model

We checked the location sensitivity of the MASI approach to different 1-D velocity models. The models were chosen by scaling the *S*-wave model by factors running from 0.8 to 2.0 (Fig. 11). This unrealistic large span covers very large velocities even beyond the corresponding *P*-wave velocity model. All epicentral location seem to be unaffected by the scaling of the velocity model. Of course, the depth of the tremor cluster (for simplicity we calculated and used the average depth for all tremor events studied) scales directly with the average velocity of the model (Fig. 11).

To study the impact of the expected three-dimensionality of the regional velocity structure at SAF, we calculated synthetics for more complex models and tried to locate the sources with MASI technique using a 1-D model. Because the regional velocity structure is not well-known (see Thurber *et al.* 2006), we used a simple 3-D model consisting of two 1-D models, differing by up to 30 per cent and placed left and right from SAF. For those models, we calculated synthetic traveltimes and applied the MASI technique using the simple 1-D model as was done for the real data. The 3-D structure introduced systematic time shifts, which resulted in mislocations (synthetic sources versus recovered locations) of the order of a few kilometres.

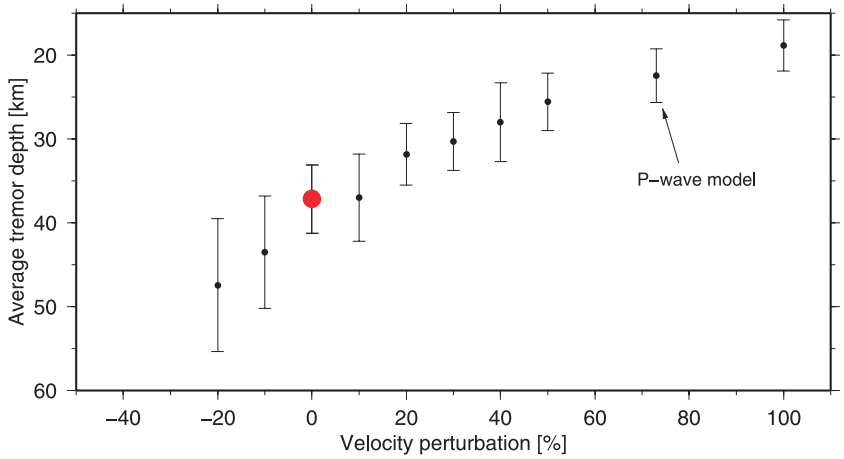

Figure 11. Test of the influence of different velocity models on the tremor depth. Shown are the average depth (black circles with error bars) of the tremor clusters from Fig. 10 with respect to the perturbation of the original model (red circle), that is 20 per cent corresponds to a velocity model 20 per cent faster than the original model (*S* wave). Note that the model with 73 per cent perturbation is equivalent to a *P*-wave model.

7.3 Calibration

We also applied a calibration procedure similar to the procedure applied by Fletcher *et al.* (2008) for UPSAR Array data by assuming that the LFE location found by Shelly *et al.* (2009) represents the correct tremor source location. We calculated synthetic traveltimes τ for all rays from the centre of the tremor locations of this study (C1) and from those of Shelly *et al.* (2009) (C2) to each station j. Station-specific time shifts δ_j are then calculated from the particular traveltime differences after subtracting the mean of the differences of each array (N is number of stations in the particular array):

$$\delta_j = (\tau_{C2,j} - \tau_{C1,j}) - \frac{1}{N}\sum_{k=1}^{N}(\tau_{C2,k} - \tau_{C1,k}). \quad (3)$$

These time shifts δ_j are then applied in the MASI technique as calibrating time shifts, that is $(t + \tau_{i,j})$ in eq. (1) is replaced by $(t + \tau_{i,j} + \delta_j)$. The table in Appendix C shows these individual calibration corrections. The calibration values show hints of anticorrelation with station elevation. This is commonly observed in California where very low velocity sediments sit at lower elevation than more compentent bedrock material. Fig. 12 shows the result of the tremor locations using those calibration values. Generally, the 'cloud' of tremor sources moves to the position derived by Shelly *et al.* (2009) and it appears to be less spatially scattered because of their shallower depth. Although some spurious outliers can be seen NE of SAF, the calibration procedure works well and thus can be used in cases of *a priori* known tremor locations.

8 RESULTS: SPATIAL AND TEMPORAL DISTRIBUTION OF NVT SOURCES

We found eight tremor events with well-defined source movements within the tremor sequence as was previously observed by Shelly *et al.* (2009). Two examples of systematic changes of tremor positions during an individual tremor event are shown in Fig. 13. Although all SAF tremor events move more or less along strike parallel to the SAF, we found four of the tremor events move northwestward and the other four move southeastward. Fig. 13 illustrates the temporal development (migration during a tremor episode) of both horizontal and vertical components of the tremor source location. Generally, all horizontal components cover the range from −25 to 25 m s^{-1}, having an average horizontal absolute velocity of around 18 m s^{-1} (negative and positive velocities correspond to movements to the NW and SE, respectively). As can be seen from Fig. 13, the scatter of the tremor source depth is too large to derive reliable vertical movement velocities, although it seems that several tremor events have the tendency to move to larger depth as time progresses.

9 DISCUSSION AND CONCLUSIONS

The MASI analysis of NVT at a set of seismic arrays has several advantages. Locations of NVT can be derived even when no LFE is found in the NVT. The use of the seismic array recordings provides high-precision locations of the NVT. With a pre-calculated table of traveltimes, an efficient and automatic detection and localization of NVT can be achieved. This could also be done as part of automated real-time monitoring of NVT on a local and regional scale. The derived epicentral locations of NVT are not sensitive to variations of the 1-D velocity models used, however, the derived source depths remain velocity model sensitive.

Prerequisite for the application of the method is the installation of a set of small-aperture arrays. Ideally, the arrays encompass the source region. Properly designed array configurations, that is with isotropic transfer functions, with a large number of stations forming the individual small-aperture arrays, and covering a large range of different inter-station distances seem to be very helpful (e.g. Haubrich 1968). Moreover, the aperture of the small-aperture arrays should be chosen in a well balanced way: small enough to account for the predominant (high) frequency content of the NVT and the limited spatial coherence of the tremor signals on the one hand, large enough to achieve the required spatial resolution to properly locate the NVT sources on the other hand. The aperture of the set of small-aperture arrays should be in the order of the source depth.

The local site structure beneath the individual array stations might distort and/or delay the wave forms possibly resulting in deviation of the beams (both in terms of azimuths and slowness) from paths predicted by the velocity model, and, thus, in potential mislocation. We show that this issue can be accounted for by applying calibration with sources of known epicentral or hypocentral position (i.e. LFE). Signals from regional events could be used to further study the mislocation behaviour of the arrays. Finally, careful selection of

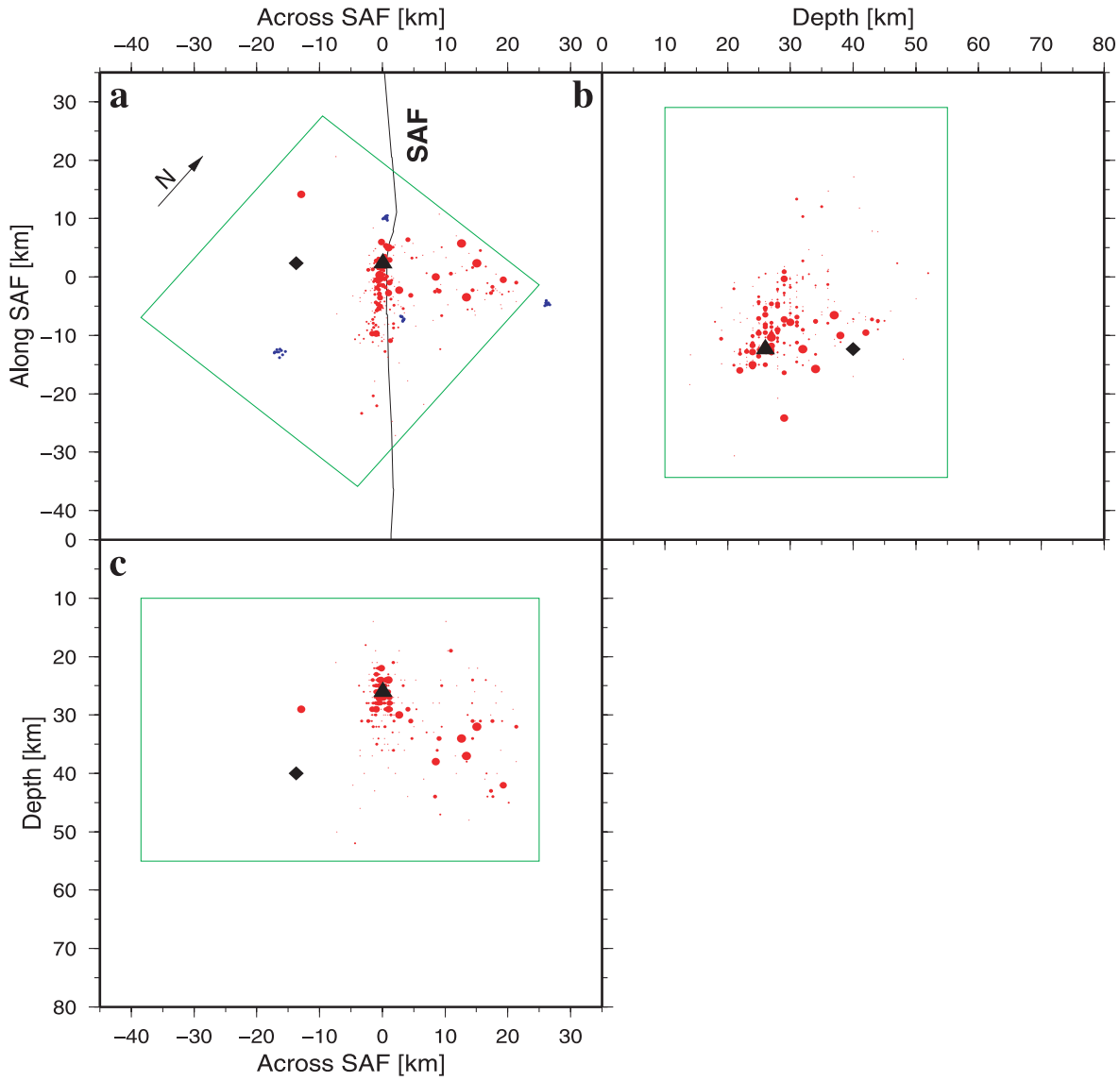

Figure 12. Rotated projection (map view and two side views) of tremor locations for all events with the calibration time shifts applied. Note that the majority of the tremor sources are now concentrated in segment of ∼20 km length and at the surface trace of the SAF. The depth of the tremor sources lies between 20 and 30 km in the lower crust and upper mantle and is curtain-shaped. The diamond indicates the location of the centre of all tremor determined without calibration, the triangle shows the approximate average location of the tremor cluster determined by Shelly *et al.* (2009). Both locations have been used to determine individual time corrections, which have been applied to calibrate the imaging method.

potential array locations (flat topography, homogeneous shallow subsurface structure, sufficient distance to faults, etc.) seems to be another key to keep disturbing influences small. Pre-site surveys of the subsurface structure (shallow seismics, H/V analysis, etc.) could be used to constrain the structure and help to select appropriate sites.

We successfully applied the MASI technique to data collected at the SAF. Despite a discrepancy of the location of the cluster of NVT sources we could confirm previous observations by Shelly *et al.* (2009). Those observations were based on the detection and localization of LFEs forming the NVT and subsequent cross-correlation of the LFE signals with several NVT sequences. The difference in the NVT source locations derived by the two methods could be accounted for by applying a calibration technique. The main observational results are that the NVT sources cluster in an almost vertical plane striking sub-parallel to the SAF, with clear source movements in both WNW–ESE and ESE–WNW directions. Whether calibration is applied or not, the sources are either at large depth of approximately ∼40 km (no calibration) or ∼26 km (with calibration), offset from the surface trace of the SAF of about ∼14 km to the W (no calibration) or beneath the surface trace (with calibration).

In any case, the tremor occurs chiefly at the transition between the locked and creeping sections of the SAF near Cholame (Murray *et al.* 2001). Less frequent tremor observations are from a region 60 km northwest of Cholame (Nadeau & Guilhem 2009). If the tremor locates within the lowermost crust (e.g. at ∼26 km depth) as indicated by the calibrated locations, it may be localized in the same frictional transition as tremor in subduction zones. Within these transition zones, there is apparently a change in fault friction from velocity weakening behaviour (that produces earthquake instabilities) and velocity strengthening behaviour (that leads to aseismic displacements). The tremor-generating process is such that small stresses (tides, passing surface waves, etc.) can trigger slip and

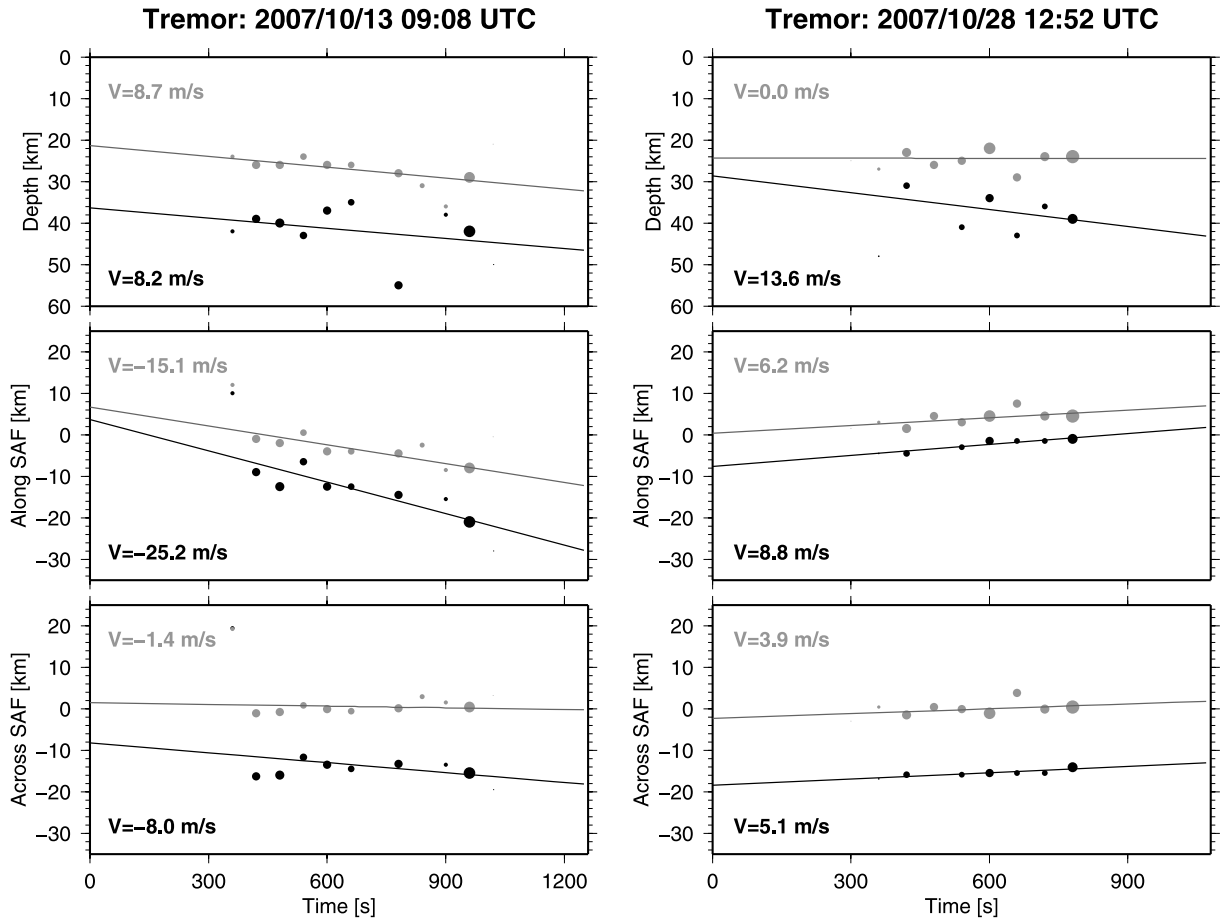

Figure 13. Two examples of tremor source localization. Shown are the time variation of the three components of the tremor source locations (time windows of 60 s) for two different tremor episodes. Black circles are the individual coordinates determined for every time window. The black lines show the least-square fitting lines and their respective velocity values. The left panel shows an event which moves in southeastern direction mainly along SAF, the right panel shows a northwestern moving tremor. Although both horizontal components show a clear trend, the depth variation during time is more scattered. Grey circles and lines show the equivalent results for the calibrated tremor source locations. Because of the shallower depth, the movements of the calibrated locations appear to be sytematically slower than the uncalibrated.

associated tremor. For a summary of conditions giving rise to tremor, see Rubinstein *et al.* (2008, 2010).

The MASI technique confirms the rapid horizontal movement of NVT sources within an episode. Movement velocities are either $\sim$18 m s^{-1} (no calibration) or $\sim$11 m s^{-1} (with calibration). These observed migration velocities are similar to those observed in the Nankai subduction zone in Japan (Shelly *et al.* 2007b), and appear to be too large to be consistent with fluid/gas migration even though fluid does appear to be present (Shelly *et al.* 2007a), and high fluid pressure appears to be associated with tremor at some locations (e.g. Samuelson *et al.* 2009). Although the propagation velocity of the tremor is orders of magnitude slower than earthquake rupture velocities (Aki & Richards 1980), the velocity is approximately an order of magnitude higher than the particle velocity in earthquakes (rate at which the sides of the fault move relative to one another). Because it is the particle velocity, not the rupture front velocity, that determines the strength of seismic radiation, it is possible that the observed 2–10 Hz energy radiates from a small region at the tremor front if the sliding region is highly localized.

The MASI method proposed here is well suited for near-real time monitoring of tremor regions (including automatic locations), both in subduction zone and strike slip regimes. Moreover, it should be well suited to provide accurate source locations necessary to further understand the nature of NVT and the relation of tremor to other mechanisms of strain release.

ACKNOWLEDGMENTS

We thank all landowners allowing us to deploy seismic stations in the Cholame region. Thanks for stimulating discussions with Malcolm Johnson. Thanks to Bob Nadeau for a recent update on tremor location and catalogue. The MT group of the GFZ, particularly Michael Becken significantly supported the field work. Jim Mechie generously calculated synthetics for testing the method. Jeanne Hardebeck and Joe Fletcher provided very helpful reviews which improved the manuscript significantly. The authors like to thank John Vidale and an anonymous reviewer for their helpful remarks. We thank Michael Weber for valuable comments on an earlier version of the paper. Instruments were provided by the GIPP (GFZ Potsdam) and the USGS. Almost all figures were made with the GMT program (Wessel & Smith 1998).

REFERENCES

Aki, K.E. & Richards, P.G., 1980. *Quantitative Seismology—Theory and Methods,* Freemann, San Francisco.

Almendros, J., Ibanez, J., Alguacil, G. & Pezzo, E., 1999. Array analysis using circular-wave-front geometry: an application to locate the nearby seismo-volcanic source, *Geophys. J. Int.,* **136,** 159–170.

Ben-Zion, Y. & Malin, P., 1991. San Andreas fault zone head waves near Parkfield, California, *Science,* **251,** 1592–1594.

Buske, S., 1999. Three-dimensional pre-stack Kirchhoff migration of deep seismic reflection data, *Geophys. J. Int.,* **137**(1), 243–260.

Chouet, B., 2003. Volcano seismology, *Pure appl. Geophys.,* **160,** 739–788.

Dahlman, O. & Israelson, H., 1977. *Monitoring Underground Nuclear Explosions,* Elsevier Scientific Publishing Company, Amsterdam.

Fletcher, J.B., Spudich, P. & Baker, L.M., 2008. Episodic Tremor at UPSAR, *AGU Fall Meeting Abstracts,* pp. C1755+.

Ghosh, A., Vidale, J.E., Sweet, J.R., Creager, K.C. & Wech, A.G., 2009. Tremor patches in Cascadia revealed by seismic array analysis, *Geophys. Res. Lett.,* **36,** L17316.

Harjes, H.-P. & Henger, M., 1973. Array-Seismologie, *Zeitschrift für Geophysik,* **39,** 865–905.

Haubrich, R.A., 1968. Array design, *Bull. seism. Soc. Am.,* **58,** 977–991.

Hole, J., Ryberg, T., Fuis, G., Bleibinhaus, F. & Sharma, A.K., 2006. Structure of the San Andreas fault zone at SAFOD from a seismic refraction survey, *Geophys. Res. Lett.,* **33,** L07312, doi:10.1029/2005GL025194.

Kao, H. & Shan, S.-J., 2004. The source-scanning algorithm: mapping the distribution of seismic sources in time and space, *Geophys. J. Int.,* **57,** 589–594.

Kao, H., Shan, S.-J., Dragert, H., Rogers, G., Cassidy, J. & Ramachandran, K., 2005. A wide depth distribution of seismic tremors along the northern Cascadia margin, *Nature,* **436**, 841–844, doi:10.1038/nature03903.

Konstantinou, K.I. & Schlindwein, V., 2002. Nature, wavefield properties and source mechanism of volcanic tremor: a review, *J. Volc. Geotherm. Res.,* **119,** 161–187.

Krüger, F. & Weber, M., 1992. The effect of low-velocity sediments on the mislocation vectors of the GRF array, *Geophys. J. Int.,* **108,** 387–393.

Krüger, F. & Ohrnberger, M., 2005a. Tracking the rupture of the Mw = 9.3 Sumatra earthquake over 1,150 km at teleseismic distance, *Nature,* **435,** 937–939.

Krüger, F. & Ohrnberger, M., 2005b. Spatio-temporal source characteristics of the 26 December 2004 Sumatra earthquake as imaged by teleseismic broadband arrays, *Geophys. Res. Lett.,* **32,** L24312, doi:10.1029/2005GL023939.

Krüger, F., Weber, M., Scherbaum, F. & Schlittenhardt, J., 1993. Double beam analysis of anomalies in the core-mantle boundary region, *J. geophys. Res.,* **20**(14), 1.475–1.478.

Krüger, F., Weber, M., Scherbaum, F. & Schlittenhardt, J., 1995. Evidence for normal and inhomogeneous lowermost mantle and core-mantle boundary structure under the Arctic and northern Canada, *Geophys. J. Int.,* **122,** 637–657.

Krüger, F., Scherbaum, F., Weber, M. & Schlittenhardt, J., 1996. Analysis of asymmetric multipathing with a generalization of the double-beam method, *Bull. seism. Soc. Am.,* **86**(3), 737–749.

Krüger, F., Baumann, M., Scherbaum, F. & Weber, M., 2001. Mid mantle scatterers near the Mariana slab detected with a double array method, *Geophys. Res. Lett.,* **28**(4), 667–670.

La Rocca, M., McCausland, W., Galluzo, D., Malone, S., Saccorotti, G. & Del Pezzo, E., 2005. Array measurements of deep tremor signals in the Cascadia subduction zone, *Geophys. Res. Lett.,* **32,** L21319, doi:10.1029/2005GL0239.

La Rocca, M., Galluzo, D., Malone, S., McCausland, W., Saccorotti, G. & Del Pezzo, E., 2008. Testing small-aperture array analysis on well-located earthquakes, and application to the location of deep tremor, *Bull. seism. Soc. Am.,* **98,** 620–635.

La Rocca, M., Creager, K.C., Galluzo, D., Malone, S., Vidale, J.E., Sweet, J.R. & Wech, A.G., 2009. Cascadia tremor located near plate interface constrained by S minus P wave times, *Science,* **323,** 620–623.

La Rocca, M., Galluzo, D., Malone, S., McCausland, W. & Del Pezzo, E., 2010. Array analysis and precise source location of deep tremor in Cascadia, *J. geophys. Res.,* **115**, B00A20, doi:10.1029/2008JB006041.

Larmat, C.S., Guyer, R.A. & Johnson, P.A., 2009. Tremor source location using time reversal: selecting the appropriate imaging field, *Geophys. Res. Lett.,* **36,** L22304, doi:10.1029/2009GL040099.

Lay, T., 1987. Analysis of near-source contributions to early *P*-wave coda for underground explosions. III. Inversion for isotropic scatterers, *Bull. seism. Soc. Am.,* **77**(5), 1.767–1.783.

Maercklin, N., Haberland, C., Ryberg, T., Weber, M., Bartov, Y. & DESERT Group, 2004. Imaging the Dead Sea Transform with scattered seismic waves, *Geophys. J. Int.,* **158,** doi:10.1111j.1365-246x.2004.02302.x.

Murray, J., Segall, P., Cervelli, P., Prescott, W. & Svarc, J., 2001. Inversion of GPS data for spatially variable slip-rate on the San Andreas Fault near Parkfield, CA, *Geophys. Res. Lett.,* **28,** 359–362.

Nadeau, R. & Dolenc, D., 2005. Nonvolcanic tremor deep beneath the San Andreas fault, *Science,* **307**, 389, doi:10.1126/science.1107142.

Nadeau, R. & Guilhem, A., 2009. Nonvolcanic tremor evolution and the San Simeon and Parkfield, California, earthquakes, *Science,* **325**, 191–193, doi:10.1126/science.1174155.

Neidell, N. & Taner, M.T., 1971. Semblance and other coherency measures for multichannel data, *Geophysics,* **36,** 482–497.

Obara, K., 2002. Nonvolcanic deep tremor associated with subduction in southwest Japan, *Science,* **296**, 1679–1681,.

Podvin, P. & Lecomte, I., 1991. Finite difference computation of traveltimes in very contrasted velocity models: a massively parallel approach and its associated tools, *Geophys. J. Int.,* **105,** 271–284.

Rentsch, S., Buske, S., Lueth, S. & Shapiro, S., 2007. Fast location of seismicity: a migration-type approach with application to hydraulic-fracturing data, *Geophysics,* **72,** S33–S40.

Rietbrock, A. & Scherbaum, F., 1999. Crustal scattering at the KTB from combined microearthquake and receiver analysis, *Geophys. J. Int.,* **136,** 57–67.

Rogers, G. & Dragert, H., 2003. Episodic tremor and slip on the Cascadia subduction zone: the chatter of silent slip, *Science,* **300,** 1842–1943.

Rubinstein, J., Rocca, M.L., Vidale, J.E., Creager, K.C. & Wech, A.G., 2008. Tidal modulation of nonvolcanic tremor, *Science,* **319**, 186–189, doi:10.1126/science.1150558.

Rubinstein, J.L., Shelly, D.R. & Ellsworth, W.L., 2010. Non-volcanic tremor: a window into the roots of fault zones, in *New Frontiers in Integrated Solid Earth Sciences,* International Year of Planet Earth, pp. 287–314, ed. S.Cloetingh, J.N., Springer, the Netherlands.

Samuelson, J., Elsworth, D. & Marone, C., 2009. Shera-induced dilatancy of fluid-saturated faults: Experiment and theory, *J. geophys. Res.,* **114,** B12404, doi:10.1029/2008JB006273.

Scherbaum, F., Krüger, F. & Weber, M., 1997. Double beam imaging: mapping lower mantle heterogeneities using combinations of source and receiver arrays, *J. geophys. Res.,* **102**(B1), 507–522.

Schneider, W., Ranzinger, K., Balch, A. & Kruse, C., 1992. A dynamic programming approach to first arrival traveltime computation in media with arbitrarily distributed velocities, *Geophysics,* **57,** 39–50.

Schneider, W.A., 1976. Integral formulation for migration in two and three dimensions, *Geophysics,* **43**(1), 49–76.

Scholz, C.H., 2002. *The Mechanics of Earthquakes and Faulting,* 2nd edn, Cambridge University Press, Cambridge, UK.

Schwartz, S. & Rokosky, J.M., 2007. Slow slip events and seismic tremor at circum-pacific subduction zones, *Rev. Geophys.,* **45,** RG3004, doi:10.1029/2006RG000208.

Schweitzer, J., 2001. Slowness corrections: one way to improve IDC products, *Pure appl. Geophys.,* **158,** 375–396.

Shelly, D.R., 2009. Possible deep fault slip preceding the 2004 Parkfield earthquake, inferred from detailed observations of tectonic tremor, *Geophys. Res. Lett.,* **36,** L17318.

Shelly, D., Beroza, G., Ide, S. & Nakamula, S., 2006. Low-frequency earthquakes in Shikoku, Japan and their relationship to episodic tremor and slip, *Nature,* **442,** 188–191.

Shelly, D., Beroza, G. & Ide, S., 2007a. Non-volcanic tremor and low frequency earthquake swarms, *Nature,* **446,** 305–307, doi:10.1038/nature 05666.

Shelly, D., Beroza, G. & Ide, S., 2007b. Complex evolution of transient slip derived from precise tremor locations in westerns Shikoku, Japan, *Geochem. Geophys. Geosyst.,* **8,** Q10014, doi:10.1029/2007GC001640.

Shelly, D., Ellsworth, W., Ryberg, T., Haberland, C., Fuis, G., Murphy, J., Nadeau, R. & Buergmann, R., 2009. Precise location of San Andreas Fault tremors near Cholame, California using seismometer clusters: slip on the deep extension of the fault?, *Geophys. Res. Lett.,* **36,** L01303, doi:10.1029/2008GL036367.

Spudich, P. & Bostwick, T., 1987. Studies of seismic coda using an earthquake cluster as a deeply buried seismograph array, *J. geophys. Res.,* **92**(B10), 10.526–10.546.

Taner, M.T. & Koehler, F., 1969. Velocity spectra-digital computer derivation and applications of velocity functions, *Geophysics,* **34,** 859–881.

Thurber, C., Zhang, H., Waldhauser, F., Hardebeck, J., Michael, A. & Eberhart-Phillips, D., 2006. Three-dimensional compressional wavespeed model, earthquake relocations, and focal mechanisms for the Parkfield, California, Region, *Bull. seism. Soc. Am.,* **96**, S38–S49, doi:10.1785/0120050825.

Thurber, C.H., Roecker, S., Roberts, K., Gold, M., Powell, L. & Rittger, K., 2003. Earthquake locations and three-dimensional fault zone structure along the creeping section of the San Andreas fault near Parkfield, CA: Preparing for SAFOD, *Geophys. Res. Lett.,* **30,** doi:10.1029/2002GL016004.

Vidale, J.E., 1988. Finite-difference calculation of traveltimes, *Bull. seism. Soc. Am.,* **78,** 2062–2076.

Vidale, J.E., 1990. Finite-difference calculation of traveltimes in three dimensions, *Geophysics,* **55,** 521–526.

Vidale, J.E. & Benz, H.M., 1992. Upper-mantle seismic discontinuities and the thermal structure of subduction zones, *Nature,* **356,** 678–683.

Wassermann, J., 1997. Locating the sources of volcanic explosions and volcanic tremor at Stromboli volcano (Italy) using beam-forming on diffraction hyperboloids, *Phys. Earth planet. Inter.,* **104,** 271–281.

Weber, M., 1994. Traveltime and amplitude anomalies at the seismic broadband array GRF, *Geophys. J. Int.,* **118,** 57–74.

Weber, M. & Wicks, C.W., 1996. Reflections from a distant subduction zone, *Geophys. Res. Lett.,* **23**(12), 1453–1456.

Wessel, P. & Smith, W., 1998. New, improved version of the Generic Mapping Tools released, *EOS, Trans. Am. geophys. Un.,* **79**, (Suppl.) 579.

APPENDIX A: PLANE-WAVE BEAMFORMING

Beamforming of traces $x_j(t)$ at station j with a particular array (formed by N stations) assuming plane-wave propagation can be formulated as follows: for a given slowness vector $\vec{u}$, time delays Θ_j at receiver j (with coordinate vector $\vec{r}_j$) can be calculated by multiplying the station distance vectors $(\vec{r}_j - \vec{r}_0)$ with the slowness vector $\vec{u}$, with r_0 being the coordinate vector of the centroid of the array (see, e.g. Krüger *et al.* 1996):

$$\Theta_j = \vec{u} \cdot \vec{r}_j. \tag{A1}$$

The time delays can then be used for the calculation of a measure for coherence (semblance; Taner & Koehler 1969; Neidell & Taner 1971) at each time T (Δ is time window in which semblance will be calculated) in a similar way as shown earlier, however, here as a function of the given slowness vector $\vec{u}$:

$$SPWB_k(\vec{u}, T) = \frac{\sum_{t=T-\Delta/2}^{T+\Delta/2} \left(\sum_{j=1}^{N} x_{k,j}(t - \Theta_j(\vec{u})) \right)^2}{N \sum_{t=T-\Delta/2}^{T+\Delta/2} \sum_{j=1}^{N} x_{k,j}^2(t - \Theta_j(\vec{u}))}. \tag{A2}$$

This calculation is performed for all time steps t for a wide range of slowness vectors. The highest semblance values indicate from which direction and with which apparent velocity coherent (tremor) energy is arriving at the particular array. Because the method is only a 3-D search (T, azimuth and slowness) and not a 4-D search as the MASI technique outlined earlier (T, three coordinates of possible source location), it is computational very efficient. Moreover, the method does not involve a velocity model. Finally, the directions corresponding to the semblance maxima of each time step derived at different arrays can be used to estimate the epicentral coordinates of the sources (cross-bearing).

APPENDIX B: ARRAY STATION LOCATIONS

Table B1. Geographic coordinates and elevations of seismic stations.

ID	Longitude (°)	Latitude (°)	Elevation (m)	ID	Longitude (°)	Latitude (°)	Elevation (m)
101	−120.33677979	35.54615926	351	201	−120.36440856	35.79662079	355
102	−120.33692319	35.53991115	359	202	−120.36426160	35.80113030	336
103	−120.33733562	35.53306861	364	203	−120.35905078	35.79557551	342
104	−120.34292263	35.54359824	380	204	−120.36719996	35.79278351	396
105	−120.34541005	35.53941670	395	205	−120.36250072	35.79762403	349
106	−120.34784923	35.53751784	414	206	−120.36189979	35.79640653	347
107	−120.35022211	35.53392002	461	207	−120.36504509	35.79521248	359
108	−120.35060992	35.53585773	465	208	−120.36651842	35.79529296	364
109	−120.35065274	35.54084647	466	209	−120.36650809	35.79795208	356
110	−120.34756532	35.54403956	477	210	−120.36558391	35.79895531	352
301	−120.04216360	35.84422849	152	401	−120.22488359	35.69456376	542
302	−120.04648733	35.84723187	157	402	−120.22355425	35.69455469	538
303	−120.04317953	35.83961081	166	403	−120.22221058	35.69454696	538
304	−120.03680566	35.84579361	148	404	−120.22089731	35.69454653	543
305	−120.04059280	35.84286027	153	405	−120.21598999	35.69417307	535
306	−120.04158527	35.84215477	158	406	−120.21602892	35.69335555	534
307	−120.04437234	35.84370627	156	407	−120.21601937	35.69254701	534
308	−120.04466295	35.84482839	162	408	−120.21600484	35.69173185	535
309	−120.04025206	35.84567769	152	409	−120.21599972	35.69092441	534
310	−120.04150240	35.84597978	152	410	−120.21599151	35.69011264	535

APPENDIX C: ARRAY ELEVATION STATICS AND CALIBRATION VALUES

Note that the recording sample interval was 5 ms.

Table C1. Elevation static and calibration corrections of seismic stations.

ID	Elevation statics (ms)	Calibration values (ms)	ID	Elevation statics (ms)	Calibration values (ms)
101	−61	126	201	−1	0
102	−54	54	202	−30	10
103	−49	−26	203	−20	38
104	−32	58	204	61	−33
105	−18	−5	205	−9	16
106	0	−42	206	−12	18
107	48	−98	207	5	−9
108	51	−78	208	12	−21
109	52	−22	209	0	−14
110	63	33	210	−5	−4
301	−3	0	401	5	−13
302	1	12	402	0	0
303	10	1	403	1	8
304	−7	−15	404	5	14
305	−2	−4	405	−1	7
306	2	−2	406	−2	0
307	0	6	407	−2	−20
308	6	7	408	−1	−6
309	−3	−5	409	−2	3
310	−3	−1	410	−2	5

APPENDIX D: 1-D-V_p VELOCITY MODEL

Poley and Eaton velocity model (ftp://ehzftp.wr.usgs.gov/klein/crust-models). This model is very similar to the average 1-D model of Thurber *et al.* (2006). The V_S model was obtained by scaling the V_P model by $\sqrt{3}$.

Table D1. One-dimensional *P*-wave velocity model.

Depth in km	V_P in km s^{-1}
0.0	2.95
0.6	3.47
1.2	4.00
1.8	4.52
2.4	5.04
3.0	5.23
3.6	5.34
4.2	5.46
4.8	5.58
5.4	5.69
6.0	5.81
8.0	6.20
10.0	6.26
12.0	6.31
14.0	6.37
16.0	6.43
18.0	6.48
20.0	6.54
22.0	6.60
24.0	6.75
26.0	7.73
28.0	8.12